



**HAL**  
open science

# Direct Quantification of Anionic Redox over Long Cycling of Li-Rich NMC via Hard X-ray Photoemission Spectroscopy

Gaurav Assat, Antonella Iadecola, Dominique Foix, Rémi Dedryvère,  
Jean-marie Tarascon

► **To cite this version:**

Gaurav Assat, Antonella Iadecola, Dominique Foix, Rémi Dedryvère, Jean-marie Tarascon. Direct Quantification of Anionic Redox over Long Cycling of Li-Rich NMC via Hard X-ray Photoemission Spectroscopy. ACS Energy Letters, 2018, 3, pp.2721 - 2728. 10.1021/acseenergylett.8b01798 . hal-01912038

**HAL Id: hal-01912038**

**<https://hal.science/hal-01912038>**

Submitted on 27 Mar 2024

**HAL** is a multi-disciplinary open access archive for the deposit and dissemination of scientific research documents, whether they are published or not. The documents may come from teaching and research institutions in France or abroad, or from public or private research centers.

L'archive ouverte pluridisciplinaire **HAL**, est destinée au dépôt et à la diffusion de documents scientifiques de niveau recherche, publiés ou non, émanant des établissements d'enseignement et de recherche français ou étrangers, des laboratoires publics ou privés.

# Direct quantification of anionic redox over long cycling of Li-rich NMC via HAXPES

Gaurav Assat,<sup>1,2,3</sup> Antonella Iadecola,<sup>2</sup> Dominique Foix,<sup>2,4</sup> Rémi Dedryvère,<sup>\*,2,4</sup> Jean-Marie Tarascon<sup>\*,1,2,3</sup>

<sup>1</sup> Collège de France, Chimie du Solide et de l'Energie - UMR 8260 CNRS, 11 Place Marcelin Berthelot, 75005 Paris, France

<sup>2</sup> Réseau sur le Stockage Electrochimique de l'Energie (RS2E) - FR CNRS 3459, 80039 Amiens Cedex, France

<sup>3</sup> Sorbonne Universités – UPMC Paris 06, 4 Place Jussieu, 75005 Paris, France

<sup>4</sup> IPREM - UMR 5254 CNRS, Université de Pau et des Pays de l'Adour, Hélioparc, 2 Avenue Pierre Angot, 64053 Pau Cedex 9, France

\*Corresponding authors:

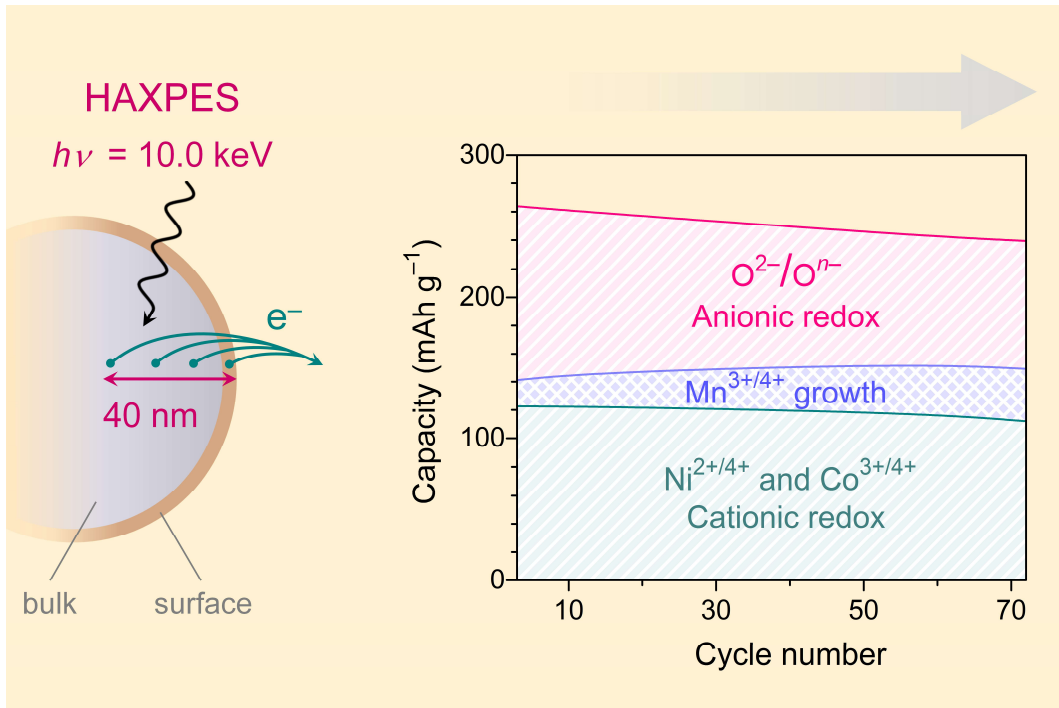
J.-M. Tarascon: [jean-marie.tarascon@college-de-france.fr](mailto:jean-marie.tarascon@college-de-france.fr) and R. Dedryvère: [remi.dedryvere@univ-pau.fr](mailto:remi.dedryvere@univ-pau.fr)

## Abstract

1 Cumulative anionic/cationic bulk redox processes are responsible for the outstanding specific  
2 energy (1000 Wh kg<sup>-1</sup>) of Li-rich Mn-based layered oxides as positive electrodes for lithium-ion  
3 batteries. Previous attempts to quantify redox processes in these materials were either limited to initial  
4 cycles or relied solely on the transition metals. It thus remains unclear to what extent does oxygen  
5 redox persist over cycling. This study provides an answer via synchrotron-based bulk-sensitive hard  
6 X-ray photoemission spectroscopy (HAXPES) by directly following the changes in electronic state  
7 of lattice oxygen over gradually increasing cycles. We find that oxygen redox contribution stabilizes  
8 after initial cycles in Li<sub>1.2</sub>Ni<sub>0.13</sub>Mn<sub>0.54</sub>Co<sub>0.13</sub>O<sub>2</sub> (Li-rich NMC) and even after 70 cycles, it accounts for  
9 more than one-third of the overall capacity. Consequently, from the quantification of Mn spectra, we  
10 observe a gradual but limited growth of Mn<sup>3+/4+</sup> redox instead of a complete activation. Partial  
11 degradation of the Ni<sup>2+/3+/4+</sup> redox is also observed. This fundamental study generates optimism for  
12 the concept of anionic redox in long-cycling batteries, and also highlights the capability of HAXPES  
13 for understanding bulk vs. surface effects in energy materials.

**Keywords.** *Batteries, Li-rich NMC, anionic redox, HAXPES*

# TOC Graphic



1 Anionic redox in transition-metal oxides has lately emerged as a promising concept of solid-  
2 state electrochemistry to design materials for energy storage and conversion.<sup>1</sup> It has unlocked the  
3 possibility to reversibly and repeatedly perform (de)intercalation reactions via the redox activity of  
4 bulk oxide anions, in addition to the conventionally utilized transition-metal redox. The energy  
5 storage limit of such oxide cathodes for rechargeable batteries has thus been increased and the  
6 materials design space has also been widened.<sup>2</sup> Subsequent to our group's fundamental investigations  
7 on 'model' materials based on 4*d* and 5*d* transition-metal layered oxides<sup>3</sup>, several studies<sup>4-11</sup> have  
8 now proven that lithium-rich manganese-based layered oxides, such as  $\text{Li}_{1.2}\text{Ni}_{0.13}\text{Mn}_{0.54}\text{Co}_{0.13}\text{O}_2$  (Li-  
9 rich NMC) that is derived from  $\text{Li}_2\text{MnO}_3$ , also exhibit combined anionic/cationic redox activity to  
10 deliver reversible capacities above  $270 \text{ mAh g}^{-1}$  and approach  $1000 \text{ Wh kg}^{-1}$  of specific energy at the  
11 material level.<sup>12-18</sup> These attributes, along with the limited use of scarce cobalt and nickel, make the  
12 Li-rich NMC family a strong competitor of today's Ni-based layered oxides<sup>19</sup> (NMCs) that are  
13 derived from  $\text{LiNiO}_2$ . NMCs are also undergoing rapid innovation owing to their promise of up to  
14  $800 \text{ Wh kg}^{-1}$  at the material level.<sup>2,12</sup> Therefore, for Li-rich cathodes to stay relevant in this duel<sup>2</sup>,  
15 several obstacles need to be eliminated – namely insufficient electrode density<sup>12</sup>, large voltage  
16 hysteresis<sup>8,20</sup>, sluggish kinetics<sup>8,21</sup>, and voltage decay upon ageing<sup>22</sup>.

17 In this study, we focus on the ageing behavior of Li-rich NMC, particularly on how the  
18 anionic/cationic redox activities evolve over cycling, which is essential for the fundamental  
19 understanding of degradation mechanisms. Most reports on anionic redox in these materials were  
20 limited to the investigation of charge-compensation in the first couple of cycles.<sup>4-11</sup> Although a recent  
21 study reported redox evolutions over long cycling, it relied on transition metals' spectra since the  
22 direct quantification of oxygen spectra was not possible.<sup>23</sup> Among the spectroscopic techniques that  
23 have been adopted by the battery community specifically for the direct characterization of oxygen  
24 redox<sup>2</sup>, two particular classes of techniques, based respectively on X-ray absorption spectroscopy  
25 (XAS) and X-ray photoemission spectroscopy (XPS), have been particularly successful in

1 demonstrating oxygen redox activity in Li-rich NMC, as summarized below.

2 Initial soft-XAS measurements in bulk-sensitive fluorescence yield mode at the O K-edge<sup>4</sup>  
3 were later repeated<sup>6,7</sup> and changes in the pre-edge intensity were assigned to changes in the electronic  
4 state of bulk oxygen. By switching to transmission mode later on, a much sharper absorption feature  
5 around 531 eV was observed and assigned to oxidized oxygen.<sup>9</sup> Such a hypothesis was complemented  
6 by obtaining O K-edge resonant inelastic X-ray scattering (RIXS) maps wherein a unique and sharp  
7 absorption–emission feature appeared on charge and disappeared on discharge.<sup>7,9</sup> This is now  
8 believed to be a signature of oxidized lattice oxygen.<sup>24</sup> RIXS was also used to show that oxygen  
9 remains active after long cycling, but further quantification could not be performed.<sup>9</sup> Concerning  
10 XPS-based results on the other hand, initial O 1s XPS spectra showed the appearance of oxidized  
11 lattice oxygen upon charging Li-rich NMC<sup>5</sup> but doubts remained due to the surface-sensitivity of  
12 standard XPS technique using Al K $\alpha$  X-ray source. We overcame this shortcoming by moving to  
13 synchrotron-based hard X-ray photoemission spectroscopy (HAXPES) for accessing bulk  
14 information and systematically explored the complete anionic/cationic charge compensation  
15 mechanism of Li-rich NMC in the first two cycles.<sup>8</sup>

16 The results from both types of direct oxygen spectroscopies have converged<sup>8,9</sup> – an important  
17 mutual conclusion being, apart from the reversibility of oxygen redox, the correct assignment of the  
18 differential capacity ( $dQ/dV$ ) discharge peak at low potential to anionic redox. The remaining task  
19 now is to investigate the effect of ageing, for which we extend herein our investigation of Li-rich  
20 NMC using HAXPES over long cycling. Taking advantage of this technique's bulk-sensitivity and  
21 quantitative nature<sup>25</sup>, we investigate the reversibility of oxygen redox during ageing and also quantify  
22 the evolution of cationic redox processes, especially Mn<sup>3+/4+</sup>. Our results present optimistic insights  
23 on the cyclability of anionic redox, and further elucidate the ageing mechanism of these practically  
24 important materials.

25  $\text{Li}_{1.2}\text{Ni}_{0.13}\text{Mn}_{0.54}\text{Co}_{0.13}\text{O}_2$  (Li-rich NMC) powders were synthesized by annealing co-

1 precipitated carbonates, as described in detail elsewhere.<sup>8,17</sup> These materials, mixed with 10 %  
2 conductive carbon, were used as positive electrodes in Swagelok-type Li half-cells. No polymeric  
3 binders were used in order to avoid decreasing the intensity of XPS signals from the active material.  
4 The electrodes exhibit, as per the 1<sup>st</sup> cycle voltage vs. composition curve recorded at 20 mA g<sup>-1</sup>  
5 (**Figure 1a**), a staircase-like charging process followed by a sloped discharge in which the capacity  
6 is 270 mAh g<sup>-1</sup>. Such an electrochemistry is typical for a good batch of Li-rich NMC. A series of  
7 identical cells was prepared and after the first activation cycle discussed above, they were continued  
8 at 40 mA g<sup>-1</sup> (circa C/6) for making long-cycled samples with gradually increasing levels of ageing.  
9 Such a relatively low C-rate is expected to uniformly age the particles and was chosen to simulate  
10 realistic ageing conditions, in contrast to fast cycling (e.g. at 1C) that may lead to non-uniform ageing  
11 besides inflating the total cycle number<sup>9</sup> and lowering the overall run-time which is known to be an  
12 important variable concerning the degradation of Li-rich NMC<sup>8,26</sup>. Fully charged and discharged  
13 samples in cycles 2, 13, 57, and 72 were thus obtained for *ex situ* HAXPES analysis, extending our  
14 previous study on only the first two cycles.<sup>8</sup> Note that a lower current of 20 mA g<sup>-1</sup> was used in the  
15 final cycle (see Experimental Methods in the Supp. Info. for further sample preparation details).  
16 **Figure 1b** shows the capacity retention for the longest cycled cell (at 40 mA g<sup>-1</sup>, circles) along with  
17 the decay of average voltage (triangles). The same graph also shows the respective capacities obtained  
18 during the final sample preparation cycles (at 20 mA g<sup>-1</sup>, stars). It is clear from **Figure 1b** that the  
19 main issue concerning the cyclability of this class of materials is the gradual fading of voltage rather  
20 than capacity retention, as we furthermore highlighted in a recent review article.<sup>2</sup> The voltage  
21 instability can also be visualized via the evolution of voltage profiles and their respective  $dQ/dV$  plots  
22 in **Figure 1c–e**. These panels also highlight the adequate repeatability with this cell configuration  
23 over the cycling durations studied herein.

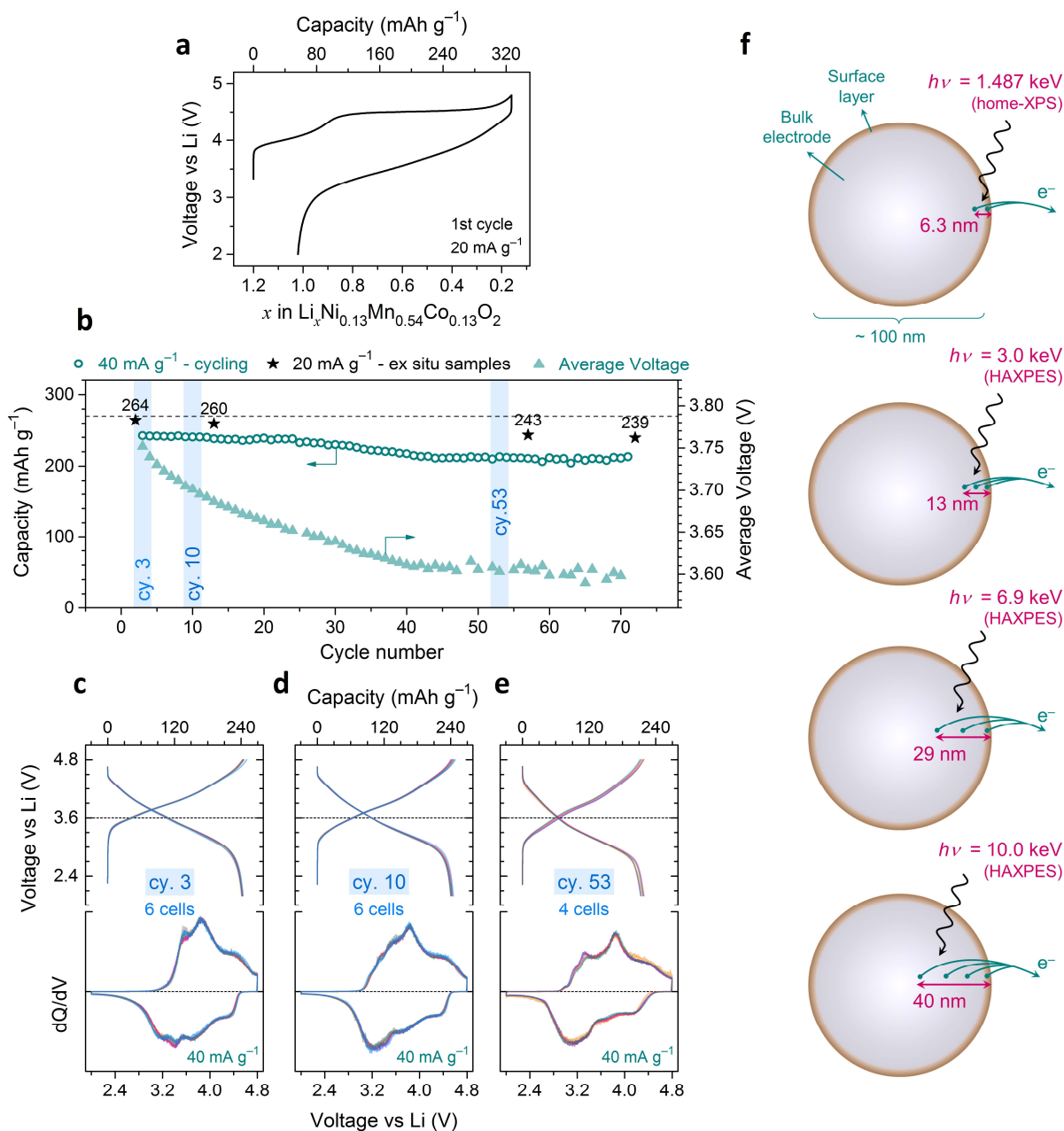


**Figure 1. Electrochemical performance of Li-rich NMC and schematic view of HAXPES probe depths.** (a) Voltage vs. composition profile in the first cycle. (b) Capacity retention (left axis) and average voltage (right axis) over long cycling. Average voltage is defined as the mean of the average charge and discharge voltages. The stars with corresponding values denote the capacities obtained during the *ex situ* sample preparation cycles. Voltage profiles and  $dQ/dV$  plots are shown for the six cells in cycle 3 (c) and 10 (d), and for the four cells in cycle 53 (e). (b) Schematic illustration of the photoelectron escape depth for surface-sensitive standard XPS (Al  $K\alpha$  X-ray source) compared with bulk-sensitive HAXPES. The primary particles are  $\sim 100 \text{ nm}$  in diameter, as characterized in the preceding work.<sup>8</sup> The probe depths, defined as three times the photoelectron inelastic mean free path<sup>27</sup>, are calculated for the O 1s core peak (calculation details in previous work<sup>8</sup> and in Supp. Info. Note S1).

1 To study the evolution of cationic and anionic redox processes over cycling, the samples were  
2 characterized with HAXPES. As schematized in **Figure 1f**, the use of high energy synchrotron  
3 radiation leads to probe depths of up to 29 nm at 6.9 keV and 40 nm at 10.0 keV, making HAXPES  
4 a bulk-sensitive technique. The O 1s HAXPES spectra are shown in **Figure 2a** for samples charged  
5 to 4.8 V and **Figure 2b** for samples discharged to 2.0 V as the cycle number increases, allowing us  
6 to directly monitor the changes in electronic state of lattice oxygen. We have previously shown that  
7 the O 1s spectrum after the first charge (**Figure 2a**, top) is characterized by an asymmetric main peak,  
8 which can be modelled by two types of lattice oxygen environments<sup>8</sup>. These are, respectively,  
9 classical lattice O<sup>2-</sup> at a binding energy (BE) of 529.5 eV and oxidized lattice oxygen O<sup>n-</sup> ( $n < 2$ , pink  
10 component at BE of 530.5). Furthermore, their ratio can be reliably quantified (% O<sup>n-</sup> = 33 %) thanks  
11 to HAXPES that leads to a diminution of polluting signals from oxygen containing surface deposits.  
12 These surface species, which arise from electrolyte and salt decomposition at the cathode electrolyte  
13 interface, are usually observed at BEs from 531.5 to 534 eV<sup>28-30</sup> and are represented by the low  
14 intensity grey peaks in **Figure 2a,b**. An additional satellite peak corresponding to the active material  
15 is also overserved (yellow) at BE = 535 eV. The main peak becomes symmetric upon discharge  
16 (**Figure 2b**, top), thus signifying the electrochemical reduction of O<sup>n-</sup> to give back O<sup>2-</sup>. Additionally,  
17 the satellite peak also disappears. For comparison, the O 1s spectra of the same samples were recorded  
18 in standard laboratory conditions (in-house XPS with  $h\nu = 1.487$  keV, Supp. Info. Figure S1). These  
19 spectra display, as expected at lower photon energy, much higher contributions of surface species  
20 relative to the lattice O<sup>2-</sup> and O<sup>n-</sup> components.

21 The 6.9 keV HAXPES spectrum of the charged sample after cycle 2 is very similar to cycle  
22 1, but with slightly less amount of oxidized oxygen (% O<sup>n-</sup> = 28 %). O<sup>n-</sup> reduces back to O<sup>2-</sup> after the  
23 second discharge. This back-and-forth appearance of O<sup>n-</sup> on charge and its disappearance on  
24 discharge demonstrates the reversibility of the anionic redox process. Note that the results obtained  
25 on cycle 2 in this study are nearly identical to our previous report<sup>8</sup>, thus underscoring the high

1 reproducibility in sample preparation and analysis. By increasing the photon energy from 6.9 keV to  
2 10.0 keV herein, a further suppression of the signal from surface species is achieved for both the  
3 charged and discharged samples. Although the  $O^{n-}$  shoulder at BE 530.5 eV is visually less evident  
4 in the charged state due to the slightly lower energy resolution at 10.0 keV, the value of %  $O^{n-}$  remains  
5 unchanged. Over long cycling,  $O^{n-}$  continues to be observed in the charged samples (**Figure 2a**),  
6 without any drastic decline in the value of %  $O^{n-}$  that stays at 25, 23, and 23 % in cycles 13, 57, and  
7 72 respectively.  $O^{2-}$  re-forms on the respective discharges (**Figure 2b**), with %  $O^{n-}$  always reducing  
8 to 9 %. Note that the contribution of surface species tends to increase after long cycling, especially  
9 on the discharged samples, which is further confirmed by in-house XPS that offers higher surface  
10 sensitivity (O 1s and C 1s in Supp. Info. Figures S1 and S2). The increase of such electrolyte / salt  
11 decomposition products upon cycling is expected to cause impedance rise and hence capacity fade  
12 under fixed current cycling. However, the exact quantification of these surface effects is not the main  
13 aim of the present study. Interestingly, the 535 eV satellite also continues to appear on charge and  
14 disappear on discharge in all pairs of long-cycled samples characterized with HAXPES. Although the  
15 fundamental origin of this satellite is yet to be understood, we believe that it might be concomitant  
16 with the  $O^{n-}$  species, especially because the same phenomenon is observed in another Li-rich oxide  
17 –  $Li_{2-x}Ru_{0.75}Sn_{0.25}O_3$ .<sup>31</sup> Further research is therefore needed to conclude whether the satellite can be  
18 ascribed as a general spectroscopic signature of oxidized oxygen. On the basis of these results that  
19 are summarized in **Figure 2c**, it can be concluded that reversible oxygen redox activity stabilizes after  
20 a few cycles and continues to persist over long cycling in Li-rich NMC. This should alleviate the  
21 apprehensions about cyclability of anionic redox in real-world batteries.

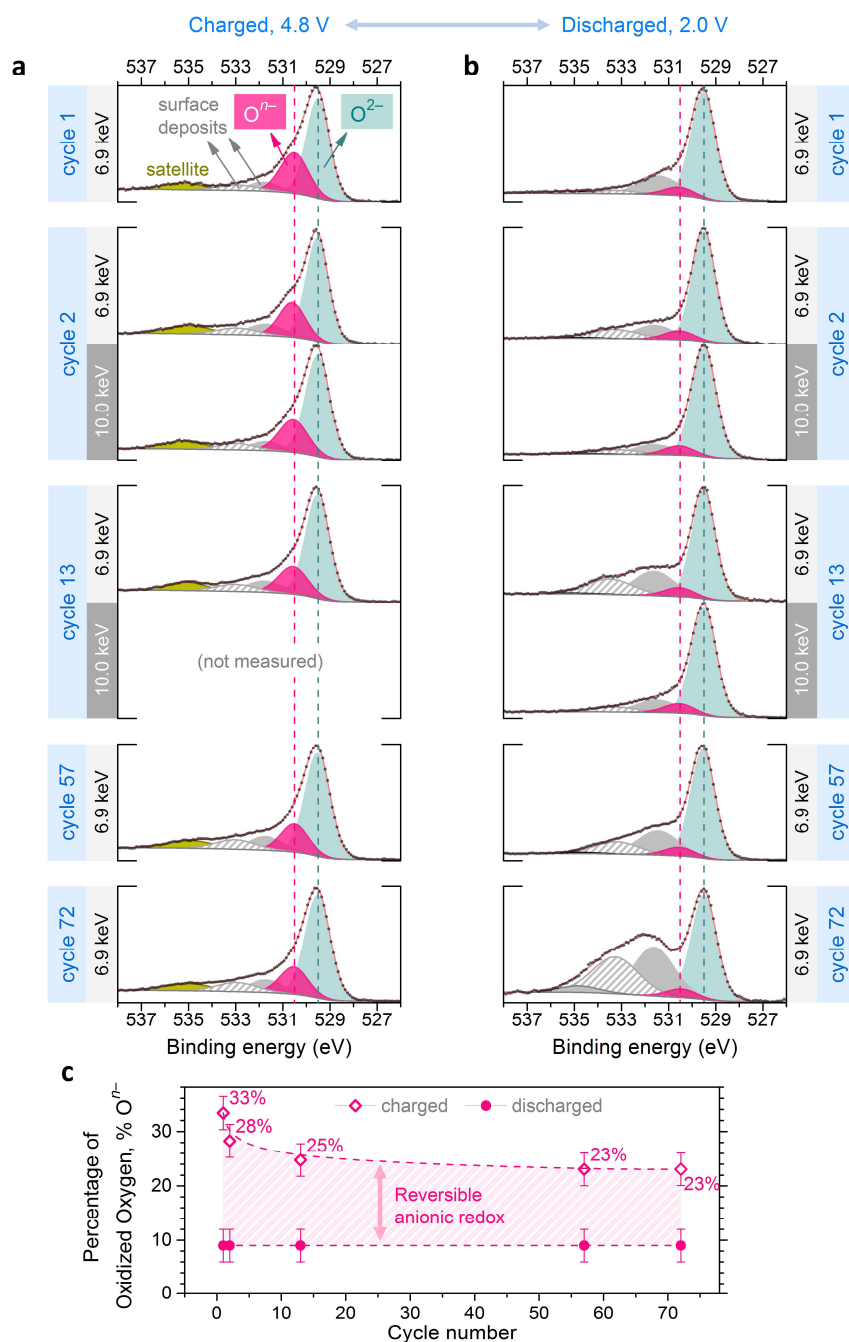


**Figure 2. Evolution of the anionic redox process over cycling.** O 1s HAXPES spectra recorded at 6.9 keV and 10.0 keV photon energies along with their respective fits for (a) the samples charged to 4.8 V and (b) discharged to 2.0 V with gradually increasing cycle numbers. The spectra for cycle 1 are the same as our previous work<sup>8</sup>, whereas the rest were measured in the present study. (c) The percentage of oxidized oxygen or % O<sup>n-</sup> ( $n < 2$ ) is plotted as a function of cycle number. It is based on the ratio of the amounts of O<sup>n-</sup> with respect to (O<sup>2-</sup> + O<sup>n-</sup>) that are estimated from the fits using integrated peak areas. % O<sup>n-</sup> is 9% for all discharged samples. The absolute error bars of  $\pm 3\%$  arise from the uncertainty in the fitting procedure that is described in detail in the preceding work.<sup>8</sup>

1 Turning now to the transition metals for understanding cationic redox, the Mn  $2p_{3/2}$  HAXPES  
2 spectra recorded at 6.9 keV are shown in **Figure 3a** for the charged and **Figure 3b** for the discharged  
3 samples. The as-synthesized material is in Mn<sup>4+</sup> state, which cannot be further oxidized on charge.  
4 We have previously shown with 3.0 keV HAXPES that on the subsequent discharge to 2.0 V, only a  
5 partial reduction of Mn<sup>4+</sup> takes place giving only 10 % Mn<sup>3+</sup> after the first discharge.<sup>8</sup> Herein, the use  
6 of 6.9 keV provides a higher probing depth as well as a better energy resolution (due to the change  
7 of monochromator). The spectrum after charging in cycle 2 (**Figure 3a**, top) is again characteristic of  
8 Mn<sup>4+</sup>. On the second discharge (**Figure 3b**, top), a clear shoulder appears on the lower BE-side of the  
9 main peak, which can be ascribed to 11 % Mn<sup>3+</sup> (purple component).<sup>32</sup> The spectra of the charged  
10 samples do not evolve much over long cycling, except for a broadening of the fine doublet structure  
11 of the main peak that may be because of gradually increasing disorder. Therefore, all spectra of  
12 charged samples are characteristic of Mn<sup>4+</sup>. On the other hand for the discharged samples, the Mn<sup>3+</sup>  
13 shoulder gradually becomes more apparent with cycling, albeit the signal from Mn<sup>4+</sup> is still  
14 predominant. It can thus be concluded that Mn<sup>3+/4+</sup> redox activity gradually augments over cycling,  
15 and quantitatively-speaking reaches 14, 21, and 22 % in cycles 13, 57, and 72 respectively, as  
16 summarized in **Figure 3c**. This systematic quantification is utilized later in the paper for determining  
17 the capacity contributions from each redox process.

18 Concerning nickel, which is the main redox-active cation in Li-rich NMC, it starts as Ni<sup>2+</sup> in  
19 the pristine material and is known to undergo the multi-electron Ni<sup>2+/3+/4+</sup> redox process over charge  
20 and discharge. Ni  $2p_{3/2}$  HAXPES at 6.9 keV was performed, as shown in **Figure 3d**, to characterize  
21 the evolution of this process. In cycle 2, a clear shift in the main peak's position can be observed  
22 between the charged to the discharged states. Moreover, the intensity and shape of the shake-up  
23 satellite can additionally be used, along with the main peak's shift, as a signature to follow the  
24 Ni<sup>2+/3+/4+</sup> process.<sup>33</sup> The charged-discharged pairs of spectra continue to display these signatures over  
25 long cycling, indicating the repeated occurrence of the Ni<sup>2+/3+/4+</sup> process. However, the charged

1 samples for cycles 57 and 72 show slight signs of reduced nickel on the main peak as well as on the  
2 satellite feature, suggesting a small under-completion of the cationic redox process after ageing of  
3 the electrodes. We exclude the possibility of significant signal contribution from reduced Ni at the  
4 surface as such reduction is limited to the first couple of nanometers<sup>34,35</sup>, which is much lower than  
5 the HAXPES probe depth. Although the signal to noise ratio is not enough for exact quantification,  
6 qualitative capacity estimation is presented later in the paper. Lastly for cobalt, the Co  $2p_{3/2}$  HAXPES  
7 spectra were recorded at 6.9 keV (Supp. Info. Figure S4) but the main peak's position remains  
8 unchanged, since it is known to be independent of Co<sup>3+/4+</sup> redox as previously shown for Li<sub>1-x</sub>CoO<sub>2</sub>.<sup>36</sup>  
9 Therefore, we rely on our previous finding based on soft-XAS<sup>8</sup> that Co<sup>3+/4+</sup> occurs concomitantly  
10 with Ni<sup>2+/3+/4+</sup> in Li-rich NMC, and assume the same herein.

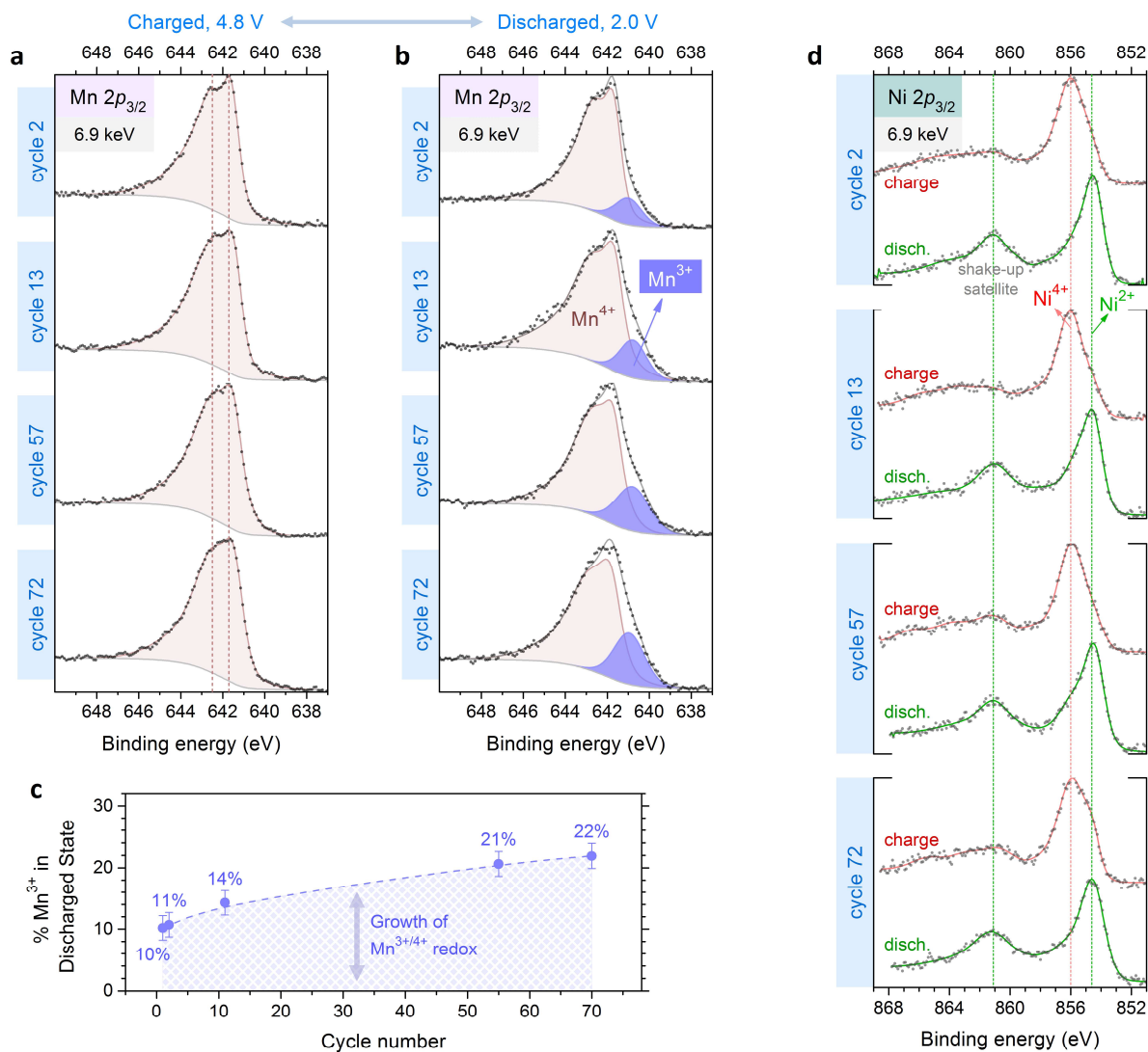


**Figure 3. Evolution of the cationic redox processes over cycling.** The Mn  $2p_{3/2}$  HAXPES spectra for (a) the samples charged to 4.8 V and (b) the samples discharged to 2.0 V. Each Mn  $2p_{3/2}$  spectrum has been fitted with two components, the first one being the spectrum of the corresponding charged sample as a reference for the Mn $^{4+}$  shape and the second one accounting for the presence of Mn $^{3+}$  at low binding energy (purple component around 641 eV). (c) The estimated amount of Mn $^{3+}$  in the discharged state is plotted as a function of cycle number. (d) The Ni  $2p_{3/2}$  HAXPES spectra are shown as charged-discharged pairs with increasing cycle number. All spectra in this Figure are recorded at 6.9 keV photon energy.

1 We now discuss the implication of our HAXPES results on the cyclability in Li-rich NMC,  
2 further dividing this issue in two parts – namely capacity retention (**Figure 4a**) and voltage fade  
3 (**Figure 4b**). Capacity-wise, out of the 264 mAh g<sup>-1</sup> delivered in the second cycle, transition metals  
4 can account for a maximum possible capacity of 141 mAh g<sup>-1</sup>, with 123 mAh g<sup>-1</sup> from the main  
5 cationic processes of Ni<sup>2+/3+/4+</sup> and Co<sup>3+/4+</sup> (complete oxidation assumed) along with 18 mAh g<sup>-1</sup> from  
6 the 10 % activity measured for Mn<sup>3+/4+</sup>. Therefore, reversible redox of bulk lattice oxygen (denoted  
7 by O<sup>2-/O<sup>n-</sup></sup>), which we have unambiguously demonstrated at probe depths of up to 40 nm  
8 (corresponding to 10.0 keV incident energy), compensates for 123 mAh g<sup>-1</sup>, i.e. nearly half of the  
9 measured capacity. We also provide direct spectroscopic proof that reversible anionic redox remains  
10 active over long cycling. Although lesser % O<sup>n-</sup> is detected in the charged state after 72 cycles, the  
11 capacity associated with it is still circa 90 mAh g<sup>-1</sup> and therefore well above one-third of the total  
12 capacity (conversion ratio to get capacity from change in % O<sup>n-</sup> is assumed same as that in cycle 2).  
13 At the same time, the growth of Mn<sup>3+/4+</sup> to 22 % corresponds just to 37 mAh g<sup>-1</sup> and the remaining  
14 capacity from nickel and cobalt (112 mAh g<sup>-1</sup>) turns out to be lower than their corresponding  
15 contribution in the initial cycles. This observation is in agreement with the evidence of incomplete  
16 nickel oxidation after long cycling (**Figure 3d**).

17 Our quantification of the long-cycling reversibility of anionic redox directly from oxygen  
18 spectroscopy is consistent with a recent study<sup>23</sup> relying on transition-metal K-edge XAS to quantify  
19 long cycling evolutions of cationic redox. The quantitative differences between the two studies likely  
20 arise from differences in the studied materials (composition or morphology), with our material  
21 showing lesser voltage fading. Nevertheless, the different techniques employed in the two works, and  
22 hence the different quantification approaches used (HAXPES on oxygen herein vs. XAS on transition  
23 metals in ref.<sup>23</sup>), make them complementary to each other. These new works provide a systematic  
24 evolution of redox processes in Li-rich NMC materials, which was only partially understood in  
25 previous literature dealing with the analysis of cycled samples using techniques mainly focused on

1 transition metal redox.<sup>34,37-42</sup> In **Figure 4a**, the diminution in oxygen capacity appears to be  
2 compensated by the buildup of  $\text{Mn}^{3+/4+}$ . This is consistent with the gradual irreversible loss of lattice  
3 oxygen, either as  $\text{O}_2$  or via chemically attacking the electrolyte, leading to material densification as  
4 the local stoichiometry partially changes from  $\text{Li}_2\text{Mn}^{4+}\text{O}_3$ -like ( $\text{O}/\text{Mn} = 3$ ) to  $\text{LiMn}^{3+}\text{O}_2$ - and  
5  $\text{LiMn}^{3+}_2\text{O}_4$ -like ( $\text{O}/\text{Mn} = 2$ ) wherein  $\text{Mn}^{3+/4+}$  is possible.<sup>6,7,40,43,44</sup> This also has implications on voltage  
6 fade, as discussed next.

7 **Figure 4b** shows the evolution of  $dQ/dV$  profiles with ageing. In general, the redox features  
8 at higher potential become less intense over cycling with the simultaneous appearance and growth of  
9 low potential processes, explaining the gradual fade in average voltage. In light of the correct redox  
10 assignments of these  $dQ/dV$  features that were performed recently<sup>8,9</sup>, we can observe the growth of  
11 low potential  $\text{Mn}^{3+/4+}$  (denoted by ‘M’) as well as a degradation in the voltage of both cationic  
12 (denoted by ‘C’) and anionic (denoted by ‘A’) redox process. Voltage fade can thus be envisaged to  
13 be a consequence of irreversible changes in the material’s overall bulk, and not simply due to surface  
14 effects, which is also supported by model-based  $dQ/dV$  analyses of up to 500 cycles<sup>45</sup> as well as long-  
15 term *in situ* diffraction data<sup>46</sup>. Eliminating voltage fade therefore calls for a paradigm-shift in  
16 designing mitigation strategies, especially since conventional strategies of surface-coating and cation-  
17 doping have only been partially effective in Li-rich NMC.<sup>12</sup>

18 In summary, by using bulk-sensitive HAXPES with up to 10.0 keV incident energy for  
19 directly following the changes in the electronic state of lattice oxygen, we have quantified the  
20 reversibility of oxygen redox to show its persistence over long cycling in Li-rich NMC. Oxygen redox  
21 compensates for almost half of the measured capacity in the initial cycles and even after the ageing  
22 duration studied for the material herein, more than one-third of the capacity still comes from  
23 reversible oxygen redox. Consequently, we observed only a gradual but limited growth of  $\text{Mn}^{3+/4+}$   
24 redox which was systematically quantified as well. A slight degradation of the  $\text{Ni}^{2+/3+/4+}$  redox was  
25 also observed. Capacity-wise, our findings serve as an optimistic prospect for the relatively nascent

1 concept of anionic redox chemistry, which can now without skepticism be envisaged for long-cycling  
 2 high-energy batteries. On the other hand, the issue of voltage fade still plagues Li-rich NMC and  
 3 appears to be bulk-related. Unconventional ideas are therefore needed to find meaningful materials'  
 4 strategies for fully eliminating voltage fade.

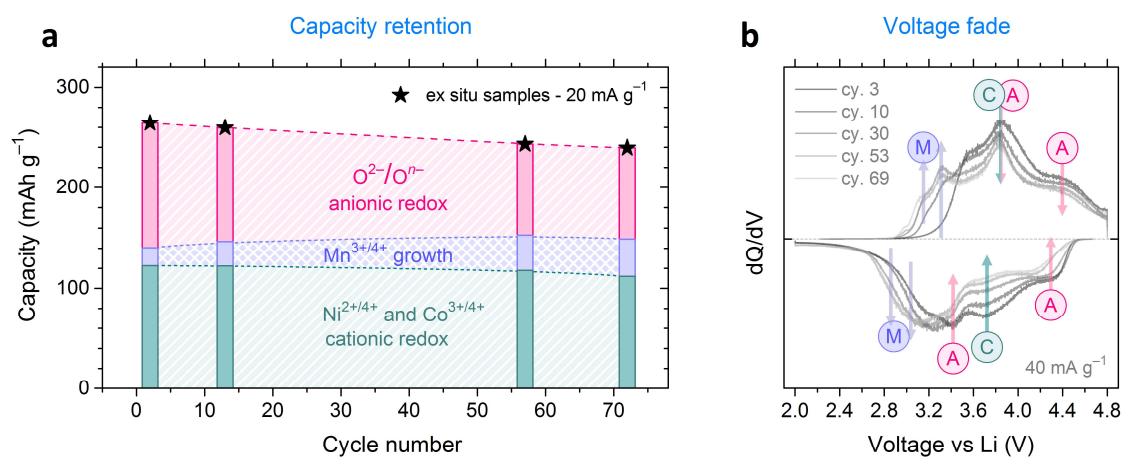


**Figure 4. Evolution of capacity and voltage of cationic and anionic redox processes over long cycling.** (a) The capacity from different redox couples is estimated from the qualitative and quantitative analysis of HAXPES spectra. (b) The evolution of different features in the  $dQ/dV$  curves is assigned to cationic 'C', or anionic 'A', or  $Mn^{3+/4+}$  'M' redox processes.

## Associated Content

1 **Supporting Information Available.** Experimental Methods, Details of HAXPES probe-depth  
2 calculations, HAXPES spectra for Co  $2p_{3/2}$ , and in-house XPS ( $h\nu = 1.487$  keV) spectra for O 1s,  
3 C 1s and F 1s.

## Acknowledgements

4 We would like to thank Yin Yang for synthesizing the pristine materials. HAXPES  
5 experiments were performed on the GALAXIES beamline<sup>47,48</sup> at SOLEIL Synchrotron, France under  
6 Proposals No. 99170166 and 20171035. We are grateful to Denis Céolin, James Ablett, and Jean-  
7 Pascal Rueff for their assistance during the experiments. J.M.T. and G.A. acknowledge the funding  
8 from European Research Council (ERC) (FP/2014)/ERC Grant-Project 670116-ARPEMA.

## Author Contributions

9 G.A and J.M.T. conceived the project. R.D. designed the HAXPES experiments. G.A.  
10 prepared the samples and performed the electrochemical measurements. G.A., A.I. and R.D. carried  
11 out the HAXPES experiments. R.D. analyzed the spectra. G.A. wrote the manuscript, which was  
12 discussed by all authors.

## Competing Financial Interests

13 The authors declare no competing financial interests.

## References

1. Grimaud, A., Hong, W. T., Shao-Horn, Y. & Tarascon, J.-M. Anionic redox processes for electrochemical devices. *Nat. Mater.* **15**, 121–126 (2016).
2. Assat, G. & Tarascon, J.-M. Fundamental understanding and practical challenges of anionic redox activity in Li-ion batteries. *Nat. Energy* 1 (2018). doi:10.1038/s41560-018-0097-0
3. Rozier, P. & Tarascon, J. M. Review—Li-Rich Layered Oxide Cathodes for Next-Generation Li-Ion Batteries: Chances and Challenges. *J. Electrochem. Soc.* **162**, A2490–A2499 (2015).
4. Oishi, M. *et al.* Direct observation of reversible charge compensation by oxygen ion in Li-rich manganese layered oxide positive electrode material,  $\text{Li}_{1.16}\text{Ni}_{0.15}\text{Co}_{0.19}\text{Mn}_{0.50}\text{O}_2$ . *J. Power Sources* **276**, 89–94 (2015).
5. Foix, D., Sathiya, M., McCalla, E., Tarascon, J.-M. & Gonbeau, D. X-ray Photoemission Spectroscopy Study of Cationic and Anionic Redox Processes in High-Capacity Li-Ion Battery Layered-Oxide Electrodes. *J. Phys. Chem. C* **120**, 862–874 (2016).
6. Luo, K. *et al.* Charge-compensation in 3d-transition-metal-oxide intercalation cathodes through the generation of localized electron holes on oxygen. *Nat. Chem.* **8**, 684–691 (2016).
7. Luo, K. *et al.* Anion Redox Chemistry in the Cobalt Free 3d Transition Metal Oxide Intercalation Electrode  $\text{Li}[\text{Li}_{0.2}\text{Ni}_{0.2}\text{Mn}_{0.6}]\text{O}_2$ . *J. Am. Chem. Soc.* **138**, 11211–11218 (2016).
8. Assat, G. *et al.* Fundamental interplay between anionic/cationic redox governing the kinetics and thermodynamics of lithium-rich cathodes. *Nat. Commun.* **8**, Article number: 2219 (2017).
9. Gent, W. E. *et al.* Coupling between oxygen redox and cation migration explains unusual electrochemistry in lithium-rich layered oxides. *Nat. Commun.* **8**, (2017).
10. Ito, A. *et al.* In situ X-ray absorption spectroscopic study of Li-rich layered cathode material  $\text{Li}[\text{Ni}_{0.17}\text{Li}_{0.2}\text{Co}_{0.07}\text{Mn}_{0.56}]\text{O}_2$ . *J. Power Sources* **196**, 6828–6834 (2011).
11. Koga, H. *et al.* Operando X-ray Absorption Study of the Redox Processes Involved upon Cycling of the Li-Rich Layered Oxide  $\text{Li}_{1.20}\text{Mn}_{0.54}\text{Co}_{0.13}\text{Ni}_{0.13}\text{O}_2$  in Li Ion Batteries. *J. Phys. Chem. C* **118**, 5700–5709 (2014).
12. Zheng, J. *et al.* Li- and Mn-Rich Cathode Materials: Challenges to Commercialization. *Adv. Energy Mater.* 1601284 (2016). doi:10.1002/aenm.201601284
13. Qiu, B. *et al.* Gas-solid interfacial modification of oxygen activity in layered oxide cathodes for lithium-ion batteries. *Nat. Commun.* **7**, 12108 (2016).
14. Kim, S., Cho, W., Zhang, X., Oshima, Y. & Choi, J. W. A stable lithium-rich surface structure for lithium-rich layered cathode materials. *Nat. Commun.* **7**, 13598 (2016).
15. Martha, S. K., Nanda, J., Veith, G. M. & Dudney, N. J. Electrochemical and rate performance

- study of high-voltage lithium-rich composition:  $\text{Li}_{1.2}\text{Mn}_{0.525}\text{Ni}_{0.175}\text{Co}_{0.1}\text{O}_2$ . *J. Power Sources* **199**, 220–226 (2012).
16. Zheng, F. *et al.* Nanoscale Surface Modification of Lithium-Rich Layered-Oxide Composite Cathodes for Suppressing Voltage Fade. *Angew. Chem. Int. Ed.* **54**, 13058–13062 (2015).
  17. Pimenta, V. *et al.* Synthesis of Li-Rich NMC: A Comprehensive Study. *Chem. Mater.* **29**, 9923–9936 (2017).
  18. Guo Haocheng *et al.* Ultrafast Heterogeneous Nucleation Enables a Hierarchical Surface Configuration of Lithium-Rich Layered Oxide Cathode Material for Enhanced Electrochemical Performances. *Adv. Mater. Interfaces* **0**, 1701465 (2018).
  19. Myung, S.-T. *et al.* Nickel-rich Layered Cathode Materials for Automotive Lithium-ion Batteries: Achievements and Perspectives. *ACS Energy Lett.* (2016).  
doi:10.1021/acsenergylett.6b00594
  20. Croy, J. R. *et al.* Examining Hysteresis in Composite  $x\text{Li}_2\text{MnO}_3 \cdot (1-x)\text{LiMO}_2$  Cathode Structures. *J. Phys. Chem. C* **117**, 6525–6536 (2013).
  21. Assat, G., Delacourt, C., Corte, D. A. D. & Tarascon, J.-M. Editors' Choice—Practical Assessment of Anionic Redox in Li-Rich Layered Oxide Cathodes: A Mixed Blessing for High Energy Li-Ion Batteries. *J. Electrochem. Soc.* **163**, A2965–A2976 (2016).
  22. Croy, J. R., Balasubramanian, M., Gallagher, K. G. & Burrell, A. K. Review of the U.S. Department of Energy's 'Deep Dive' Effort to Understand Voltage Fade in Li- and Mn-Rich Cathodes. *Acc. Chem. Res.* **48**, 2813–2821 (2015).
  23. Hu, E. *et al.* Evolution of redox couples in Li- and Mn-rich cathode materials and mitigation of voltage fade by reducing oxygen release. *Nat. Energy* **1** (2018). doi:10.1038/s41560-018-0207-z
  24. Yang, W. & Devereaux, T. P. Anionic and cationic redox and interfaces in batteries: Advances from soft X-ray absorption spectroscopy to resonant inelastic scattering. *J. Power Sources* **389**, 188–197 (2018).
  25. Philippe, B. *et al.* Photoelectron spectroscopy for lithium battery interface studies. *J. Electrochem. Soc.* **163**, A178–A191 (2016).
  26. Bettge, M. *et al.* Voltage Fade of Layered Oxides: Its Measurement and Impact on Energy Density. *J. Electrochem. Soc.* **160**, A2046–A2055 (2013).
  27. Tanuma, S., Powell, C. J. & Penn, D. R. Calculations of electron inelastic mean free paths. IX. Data for 41 elemental solids over the 50 eV to 30 keV range. *Surf. Interface Anal.* **43**, 689–713 (2011).
  28. Edström, K., Gustafsson, T. & Thomas, J. O. The cathode–electrolyte interface in the Li-ion battery. *Electrochimica Acta* **50**, 397–403 (2004).

29. Dedryvère, R. *et al.* XPS Identification of the Organic and Inorganic Components of the Electrode/Electrolyte Interface Formed on a Metallic Cathode. *J. Electrochem. Soc.* **152**, A689 (2005).
30. Ouatani, L. E. *et al.* The Effect of Vinylene Carbonate Additive on Surface Film Formation on Both Electrodes in Li-Ion Batteries. *J. Electrochem. Soc.* **156**, A103–A113 (2009).
31. Assat, G., Iadecola, A., Delacourt, C., Dedryvère, R. & Tarascon, J.-M. Decoupling Cationic–Anionic Redox Processes in a Model Li-rich Cathode via Operando X-ray Absorption Spectroscopy. *Chem. Mater.* (2017). doi:10.1021/acs.chemmater.7b03434
32. Azmi, R. *et al.* Surface analytical approaches to reliably characterize lithium ion battery electrodes. *Surf. Interface Anal.* **50**, 43–51 (2018).
33. Doubaji, S. *et al.* Passivation Layer and Cathodic Redox Reactions in Sodium-Ion Batteries Probed by HAXPES. *ChemSusChem* **9**, 97–108 (2016).
34. Zheng, J. *et al.* Structural and Chemical Evolution of Li- and Mn-Rich Layered Cathode Material. *Chem. Mater.* **27**, 1381–1390 (2015).
35. Lin, F. *et al.* Surface reconstruction and chemical evolution of stoichiometric layered cathode materials for lithium-ion batteries. *Nat. Commun.* **5**, 3529 (2014).
36. Dahéron, L. *et al.* Electron Transfer Mechanisms upon Lithium Deintercalation from LiCoO<sub>2</sub> to CoO<sub>2</sub> Investigated by XPS. *Chem. Mater.* **20**, 583–590 (2008).
37. Yang, F. *et al.* Nanoscale Morphological and Chemical Changes of High Voltage Lithium–Manganese Rich NMC Composite Cathodes with Cycling. *Nano Lett.* **14**, 4334–4341 (2014).
38. Wu, Y. *et al.* Probing the initiation of voltage decay in Li-rich layered cathode materials at the atomic scale. *J. Mater. Chem. A* **3**, 5385–5391 (2015).
39. Yabuuchi, N., Kubota, K., Aoki, Y. & Komaba, S. Understanding Particle-Size-Dependent Electrochemical Properties of Li<sub>2</sub>MnO<sub>3</sub>-Based Positive Electrode Materials for Rechargeable Lithium Batteries. *J. Phys. Chem. C* **120**, 875–885 (2016).
40. Hong, J., Gwon, H., Jung, S.-K., Ku, K. & Kang, K. Review—Lithium-Excess Layered Cathodes for Lithium Rechargeable Batteries. *J. Electrochem. Soc.* **162**, A2447–A2467 (2015).
41. Hy, S. *et al.* Understanding the Role of Ni in Stabilizing the Lithium-Rich High-Capacity Cathode Material Li[Ni<sub>x</sub>Li<sub>(1–2x)</sub>/3Mn<sub>(2–x)</sub>/3]O<sub>2</sub> (0 ≤ x ≤ 0.5). *Chem. Mater.* **26**, 6919–6927 (2014).
42. Hy, S., Su, W.-N., Chen, J.-M. & Hwang, B.-J. Soft X-ray Absorption Spectroscopic and Raman Studies on Li<sub>1.2</sub>Ni<sub>0.2</sub>Mn<sub>0.6</sub>O<sub>2</sub> for Lithium-Ion Batteries. *J. Phys. Chem. C* **116**, 25242–25247 (2012).
43. Strehle, B. *et al.* The Role of Oxygen Release from Li- and Mn-Rich Layered Oxides during the

- First Cycles Investigated by On-Line Electrochemical Mass Spectrometry. *J. Electrochem. Soc.* **164**, A400–A406 (2017).
44. Wandt, J., Freiberg, A. T. S., Ogorodnik, A. & Gasteiger, H. A. Singlet oxygen evolution from layered transition metal oxide cathode materials and its implications for lithium-ion batteries. *Mater. Today* (2018). doi:10.1016/j.mattod.2018.03.037
45. Rinaldo, S. G. *et al.* Physical Theory of Voltage Fade in Lithium-and Manganese-Rich Transition Metal Oxides. *J. Electrochem. Soc.* **162**, A897–A904 (2015).
46. Kleiner, K. *et al.* Origin of High Capacity and Poor Cycling Stability of Li-Rich Layered Oxides: A Long-Duration in Situ Synchrotron Powder Diffraction Study. *Chem. Mater.* **30**, 3656–3667 (2018).
47. Rueff, J.-P. *et al.* The GALAXIES beamline at the SOLEIL synchrotron: inelastic X-ray scattering and photoelectron spectroscopy in the hard X-ray range. *J. Synchrotron Radiat.* **22**, 175–179 (2015).
48. Rueff, J.-P., Rault, J. E., Ablett, J. M., Utsumi, Y. & Céolin, D. HAXPES for Materials Science at the GALAXIES Beamline. *Synchrotron Radiat. News* **31**, 4–9 (2018).

# Direct quantification of anionic redox over long cycling of Li-rich NMC via HAXPES

Gaurav Assat,<sup>1,2,3</sup> Antonella Iadecola,<sup>2</sup> Dominique Foix,<sup>2,4</sup> Rémi Dedryvère,<sup>\*,2,4</sup> Jean-Marie Tarascon<sup>\*,1,2,3</sup>

<sup>5</sup> Collège de France, Chimie du Solide et de l'Energie - UMR 8260 CNRS, 11 Place Marcelin Berthelot, 75005 Paris, France

<sup>6</sup> Réseau sur le Stockage Electrochimique de l'Energie (RS2E) - FR CNRS 3459, 80039 Amiens Cedex, France

<sup>7</sup> Sorbonne Universités – UPMC Paris 06, 4 Place Jussieu, 75005 Paris, France

<sup>8</sup> IPREM - UMR 5254 CNRS, Université de Pau et des Pays de l'Adour, Hélioparc, 2 Avenue Pierre Angot, 64053 Pau Cedex 9, France

\*Corresponding authors:

J.-M. Tarascon: [jean-marie.tarascon@college-de-france.fr](mailto:jean-marie.tarascon@college-de-france.fr) and R. Dedryvère: [remi.dedryvere@univ-pau.fr](mailto:remi.dedryvere@univ-pau.fr)

## Supporting Information

## Experimental Methods

1           **Material synthesis and characterization.**  $\text{Li}_{1.2}\text{Ni}_{0.13}\text{Mn}_{0.54}\text{Co}_{0.13}\text{O}_2$  (Li-rich NMC) powders  
2 were synthesized with a two-step process involving carbonate co-precipitation followed by heat  
3 treatment.<sup>1</sup> Note that we used the same batch of material as in our previous paper.<sup>2</sup> First,  
4 stoichiometric Ni-Mn-Co carbonate was co-precipitated from an aqueous solution of transition-metal  
5 sulphates by introducing in it an aqueous solution of sodium carbonate (2 M) and ammonia (0.2 M).  
6 This was carried out in a controlled manner (pH = 8, T = 55 °C, stirring speed = 1000 rpm) by using  
7 a continuously stirred tank reactor (Bioflow 320, Eppendorf) to regulate the morphology and  
8 homogeneity of particles. The resulting Ni-Mn-Co carbonate powders were heat treated with  $\text{Li}_2\text{CO}_3$   
9 at 850°C for 12 hours to obtain the Li-rich NMC powders with a primary particle size of ~100 nm as  
10 characterized by SEM (FEI Helios NanoLab 650). The crystal structure was confirmed with X-ray  
11 diffraction (BRUKER D8 Advance diffractometer with  $\text{Cu K}\alpha$  radiation) and the targeted elemental  
12 composition was verified with inductively coupled plasma – mass spectrometry.

13           **Ex situ sample preparation.** Li half-cells having Li-rich NMC powders hand mixed (to  
14 preserve morphology) with conductive Carbon Super P in a 90:10 ratio at the positive electrode (total  
15 weight kept ~12 mg for each cell to ensure repeatability) and Li metal foil at the negative electrode  
16 were assembled in Swagelok-type cells in an Argon glovebox ( $\text{O}_2 < 0.1$  ppm,  $\text{H}_2\text{O} < 0.1$  ppm). The  
17 positive and negative electrodes were separated with two layers of Whatman GF/D borosilicate glass-  
18 fiber sheets along with two layers of Cellguard separators soaked with an electrolyte – LP100 (Merck)  
19 having 1 M  $\text{LiPF}_6$  dissolved in ethylene carbonate : propylene carbonate : dimethyl carbonate in a 1  
20 : 1 : 3 weight ratio. Note that Swagelok cells were preferred to coin-cells due to the possible risk of  
21 short-circuit during the coin-cell disassembly process that could lead to artificial reduction of the  
22 positive electrode. All cells were rested for 2 hours before testing. The first charge-discharge cycle  
23 was performed at a constant specific current of 20  $\text{mA g}^{-1}$ . Then, long cycling was performed at 40  
24  $\text{mA g}^{-1}$  (circa C/6). After achieving the desired number of cycles, the final sample preparation cycle  
25 was performed at a lower specific current of 20  $\text{mA g}^{-1}$  to reach either the full charged (4.8 V) or the  
26 full discharged (2.0 V) states.

27           Upon achieving these states, the Swagelok cells were carefully disassembled in the glovebox  
28 (ensuring no short circuiting) and as soon as possible (to prevent self-discharge under open circuit).  
29 The positive electrode powders were rinsed thoroughly three times with anhydrous dimethyl  
30 carbonate (DMC) to get rid of the electrolyte and soluble surface deposits. DMC was evaporated by  
31 leaving the samples in vacuum (using the glovebox antechamber) for at least 1 hour. Note that our *ex*  
32 *situ* electrode samples were recovered as loose powders that were thoroughly mixed. This averaged

1 out any concentration gradients which can bias XPS results if slurry-electrodes are used instead.

2 **Sample handling and transfer.** Great attention was paid to preserve the samples from air  
3 and moisture exposure during transfer and handling. They were constantly maintained in dry argon  
4 atmosphere or in vacuum. Inside the glovebox, the recovered *ex situ* powders were pasted on carbon  
5 tapes stuck on a sample holder. For HAXPES, they were transferred from the on-site argon glovebox  
6 to the beamline introduction chamber (that was kept under vacuum) via a specially-designed  
7 detachable stainless-steel vacuum transfer system ('suitcase'). The samples were first sealed in this  
8 'suitcase' inside the glovebox and then transferred to the beamline within 15 minutes.

9 **Hard X-ray Photoemission Spectroscopy (HAXPES).** HAXPES measurements were  
10 carried out at the GALAXIES<sup>3,4</sup> beamline of SOLEIL synchrotron facility in France. Photon  
11 excitation energies  $h\nu = 6.9$  and  $10.0$  keV were obtained from the third order reflection of the Si(111)  
12 double-crystal monochromator. Photoelectrons were analyzed by a SCIENTA EW4000 spectrometer,  
13 and the obtained energy resolution from the Au Fermi edge was  $0.14$  eV for  $6.9$  keV and  $0.22$  eV for  
14  $10.0$  keV photon energy. No charge neutralizer was used. The analysis chamber pressure was  
15 maintained around  $10^{-8}$  mbar during the measurements. The binding energy scale was calibrated to  
16 match the in-house XPS spectra on the same samples.

17 **In-house X-ray Photoemission Spectroscopy (XPS).** XPS measurements were performed  
18 with a Kratos Axis Ultra spectrometer, using a focused monochromatized Al  $K\alpha$  radiation ( $h\nu =$   
19  $1486.6$  eV). The analyzed area of the samples was  $300 \mu\text{m} \times 700 \mu\text{m}$ . Peaks were recorded with  
20 constant pass energy of  $20$  eV. For the Ag  $3d_{5/2}$  line, the full width at half maximum (FWHM) was  
21  $0.58$  eV under the recording conditions. No charge neutralization was required and the pressure was  
22 maintained around  $10^{-8}$  mbar. The binding energy scale was calibrated from the C  $1s$  core peak at  
23  $284.4$  eV coming from Carbon Super P added to the positive electrode materials.

## Supplementary Note S1

1           **Calculation of XPS and HAXPES probe depths.** The probe depths are defined as three  
2 times the photoelectron inelastic mean free path (IMFP), and were estimated from the TPP-2M model  
3 developed by Tanuma *et al.*<sup>5</sup> This model uses four parameters: (1) the formula molecular weight, (2)  
4 the density, (3) the number of valence electrons per formula, (4) the band gap. Given the composition  
5 of the material  $\text{Li}_{1.2}\text{Ni}_{0.13}\text{Mn}_{0.54}\text{Co}_{0.13}\text{O}_2$ , its molecular weight is  $85.29 \text{ g mol}^{-1}$  and the number of  
6 valence electrons is 19.45 per formula. The density is  $4.18 \text{ g cm}^{-3}$ . The band gap is unknown, but this  
7 parameter has only little influence on the final result (for example, the calculated probe depth for  $h\nu$   
8 = 6900 eV is 29 nm using band gap = 0 eV and 30 nm using band gap = 5 eV). The band gap was  
9 fixed to 2 eV for the calculations. The calculated values are as follows:

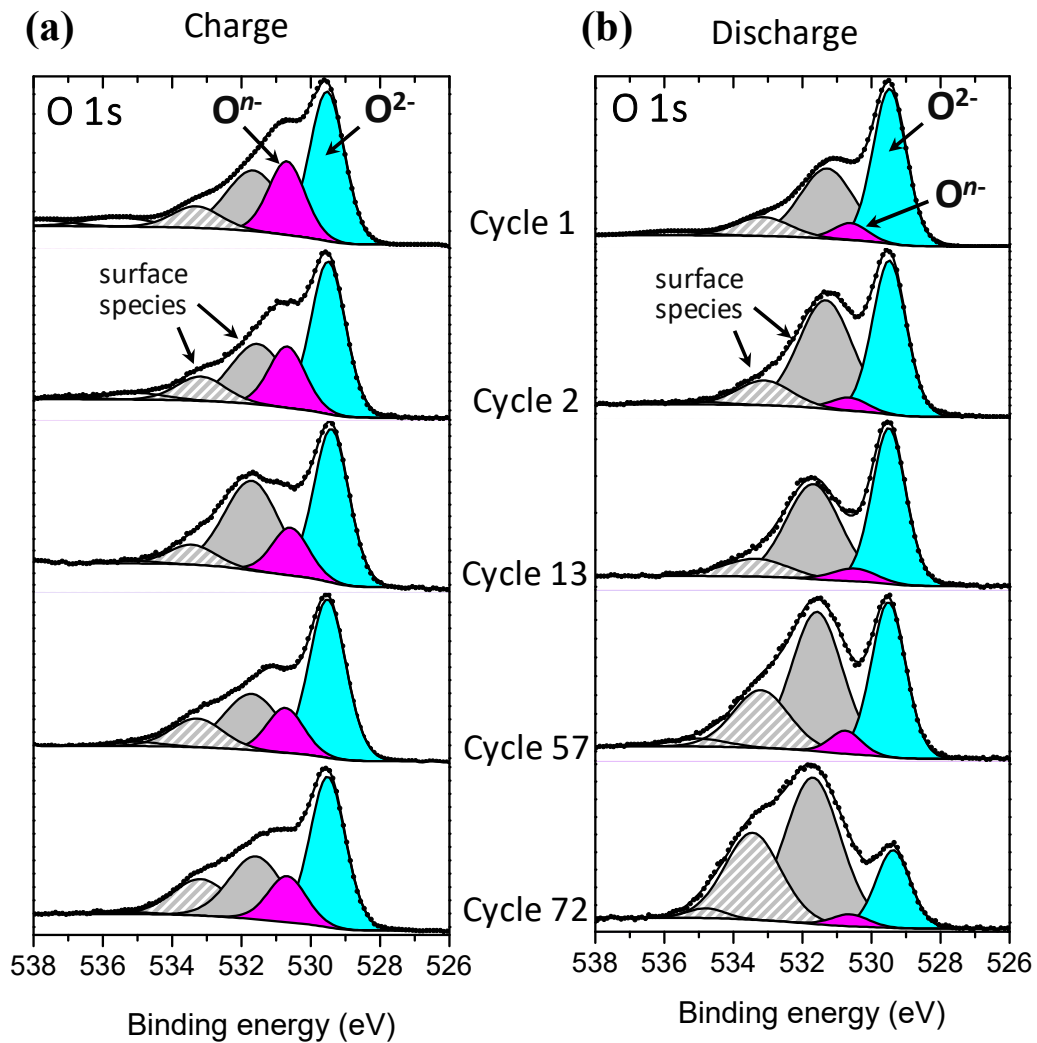
10

Photon energy (keV)	Probe depth (nm)			
	O 1s	Mn 2p	Co 2p	Ni 2p
1.487	6.3	5.7	5.0	4.6
3.0	13	13	12	12
6.9	29	28	28	28
10.0	40	40	39	39

11

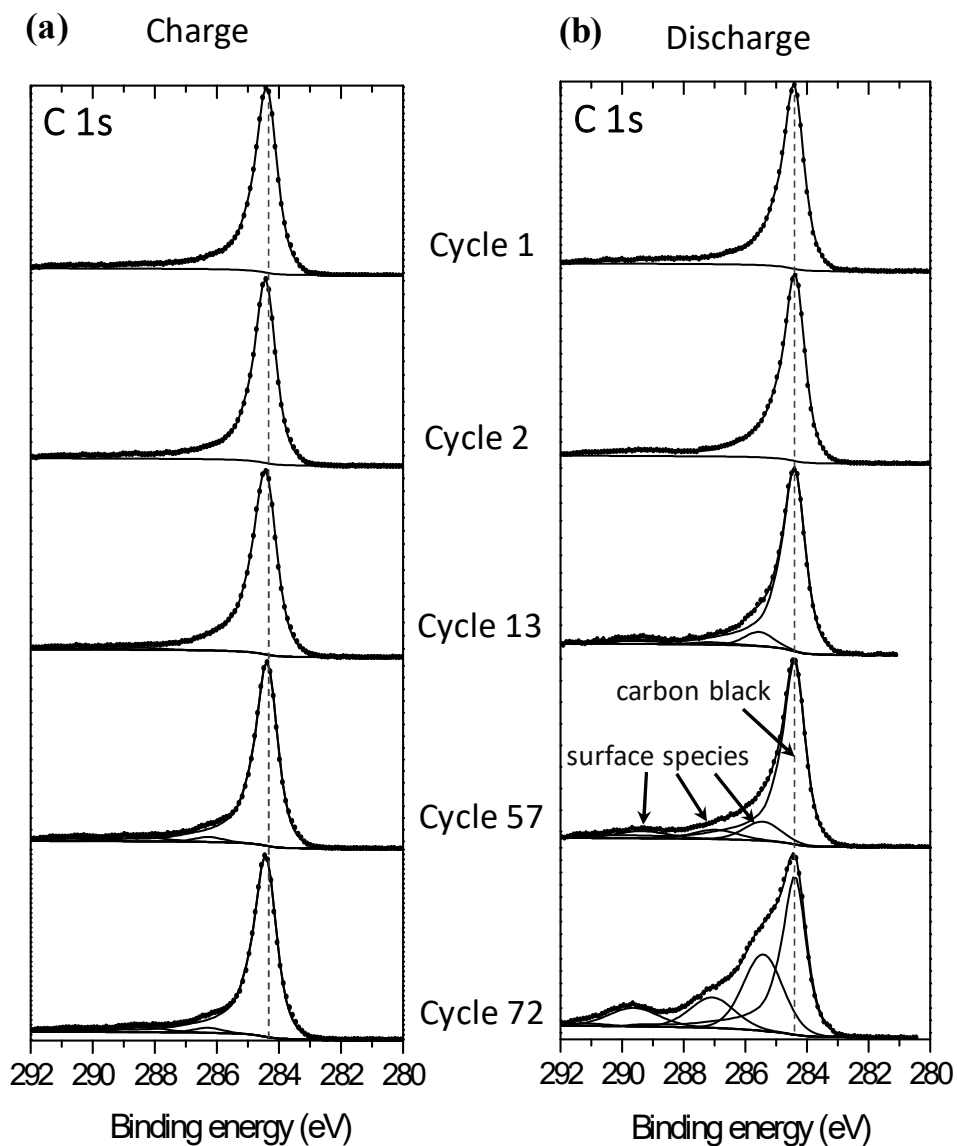
12

## Supplementary Figure S1



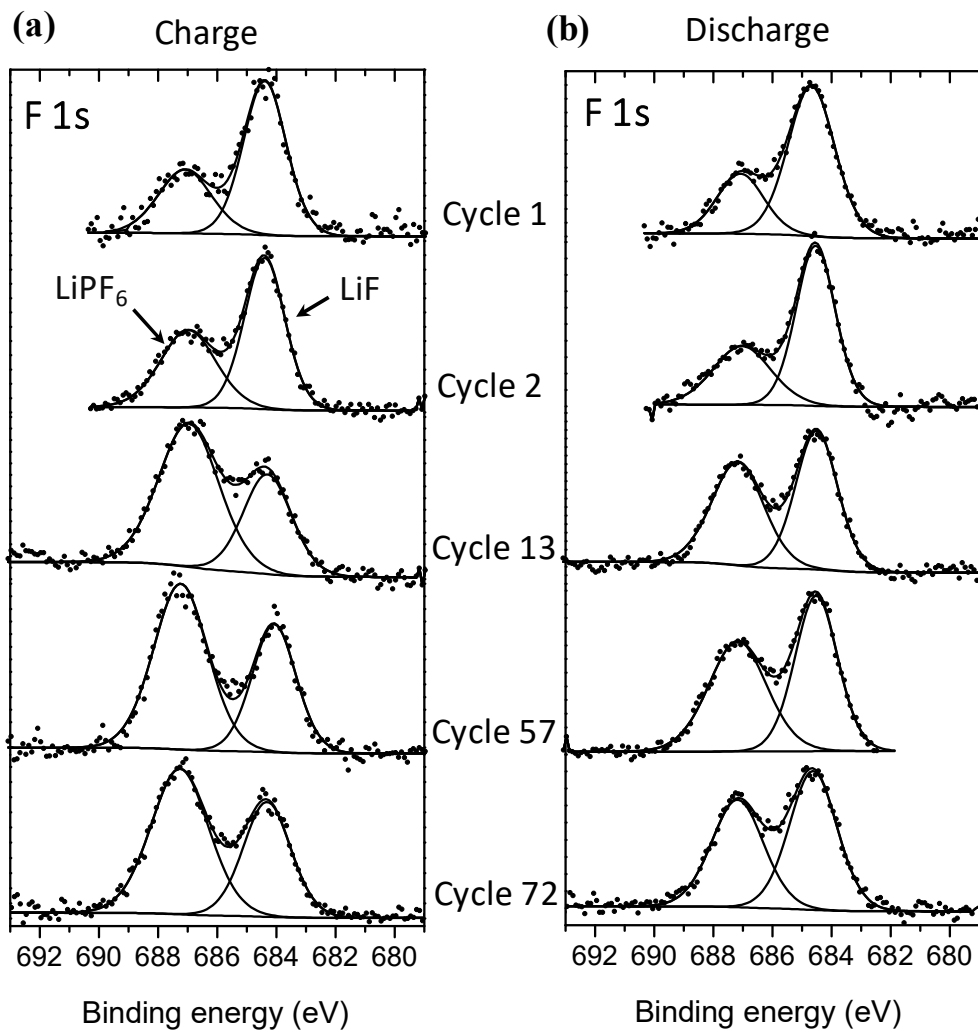
1 **Evolution of the anionic redox process over cycling.** O 1s in-house XPS spectra recorded at  
2 1.487 keV: (a) samples charged to 4.8 V and (b) samples discharged to 2.0 V with gradually  
3 increasing cycle numbers.

## Supplementary Figure S2



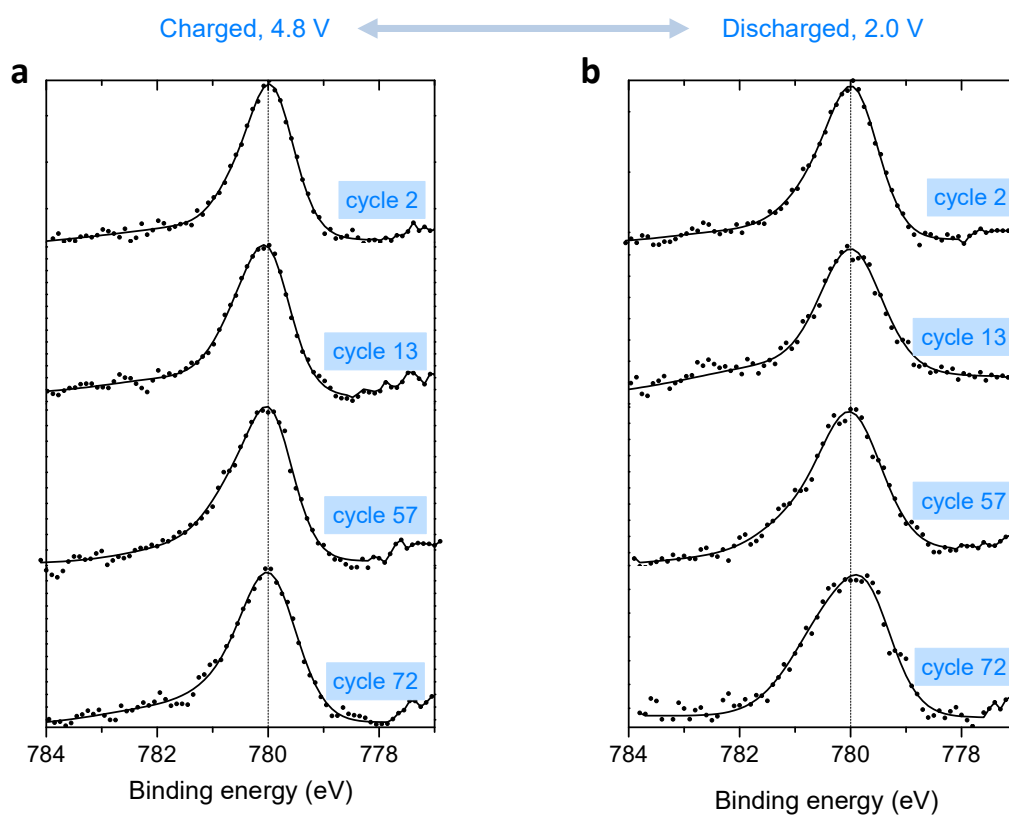
**C 1s in-house XPS spectra recorded at 1.487 keV: (a) samples charged to 4.8 V and (b) samples discharged to 2.0 V with gradually increasing cycle numbers. The position of the carbon black peak at 284.4 eV was taken as reference for binding energy calibration.**

### Supplementary Figure S3



**F 1s in-house XPS spectra recorded at 1.487 keV: (a) samples charged to 4.8 V and (b) samples discharged to 2.0 V with gradually increasing cycle numbers.**

## Supplementary Figure S4



**Evolution of Co  $2p_{3/2}$  over cycling.** The main peak of Co  $2p_{3/2}$  HAXPES spectra recorded at 6.9 keV for (a) the samples charged to 4.8 V and (b) the samples discharged to 2.0 V. There is no shift in the main peak's position between charge and discharge. However, this cannot be interpreted as an absence of participation of cobalt to the redox process, since the main peak binding energy is the same for  $\text{Co}^{3+}$  and  $\text{Co}^{4+}$ , as shown previously for  $\text{Li}_{1-x}\text{CoO}_2$ .<sup>6</sup>

1  
2  
3

## Supporting References

1. Pimenta, V. *et al.* Synthesis of Li-Rich NMC: A Comprehensive Study. *Chem. Mater.* **29**, 9923–9936 (2017).
2. Assat, G. *et al.* Fundamental interplay between anionic/cationic redox governing the kinetics and thermodynamics of lithium-rich cathodes. *Nat. Commun.* **8**, Article number: 2219 (2017).
3. Rueff, J.-P. *et al.* The GALAXIES beamline at the SOLEIL synchrotron: inelastic X-ray scattering and photoelectron spectroscopy in the hard X-ray range. *J. Synchrotron Radiat.* **22**, 175–179 (2015).
4. Rueff, J.-P. *et al.* HAXPES for Materials Science at the GALAXIES Beamline. *Synchrotron Radiat. News* **31**, 4–9 (2018).
5. Tanuma, S., Powell, C. J. & Penn, D. R. Calculations of electron inelastic mean free paths. IX. Data for 41 elemental solids over the 50 eV to 30 keV range. *Surf. Interface Anal.* **43**, 689–713 (2011).
6. Dahéron, L. *et al.* Electron Transfer Mechanisms upon Lithium Deintercalation from LiCoO<sub>2</sub> to CoO<sub>2</sub> Investigated by XPS. *Chem. Mater.* **20**, 583–590 (2008).